Biomimetic apatite sintered at very low temperature by spark plasma sintering: Physico-chemistry and microstructure aspects

David Grossin [a,*], Sabrina Rollin-Martinet [a,c], Claude Estournès [a,b], Fabrice Rossignol [c], Eric Champion [c], Christèle Combes [a], Christian Rey [a], Chevallier Geoffroy [b], Christophe Drouet [a]

[a] CIRIMAT, Université de Toulouse, CNRS/INPT/UPS, ENSIACET 118 route de Narbonne, 31077 Toulouse Cedex 4, France
[b] PNF[2], CNRS/UPS, MHT, 118 Route de Narbonne, 31062 Toulouse, France
[c] SPCTS, CNRS/Université de Limoges, Faculté des Sciences et Techniques, 123 Avenue Albert Thomas, 87060 Limoges Cedex, France

Article history:
Received 14 April 2009
Received in revised form 16 July 2009
Accepted 6 August 2009
Available online 15 August 2009

Keywords:
Apatites
Resorbable bioceramics
Spark plasma sintering
Low-temperature sintering

A B S T R A C T

Nanocrystalline apatites analogous to bone mineral are very promising materials for the preparation of highly bioactive ceramics due to their unique intrinsic physico-chemical characteristics. Their surface reactivity is indeed linked to the presence of a metastable hydrated layer on the surface of the nanocrystals. Yet the sintering of such apatites by conventional techniques, at high temperature, strongly alters their physico-chemical characteristics and biological properties, which points out the need for "softer" sintering processes limiting such alterations. In the present work a non-conventional technique, spark plasma sintering, was used to consolidate such nanocrystalline apatites at non-conventional, very low temperatures ($T < 300$ °C) so as to preserve the surface hydrated layer present on the nanocrystals. The bioceramics obtained were then thoroughly characterized by way of complementary techniques. In particular, microstructural, nanostructural and other major physico-chemical features were investigated and commented on. This work adds to the current international concern aiming at improving the capacities of present bioceramics, in view of elaborating a new generation of resorbable and highly bioactive ceramics for bone tissue engineering.

1. Introduction

Hydroxyapatite (HAP), $Ca_{10}(PO_4)_6(OH)_2$, is one of the most widely used bioceramics for bone and tooth substitution due to a structural similarity to the mineral part of calcified tissues. In fact, bone mineral is mostly composed of carbonated nanocrystalline apatites corresponding to the general formula $Ca_{10-(x-u)}(PO_4)_{6-x}(HPO_4, CO_3)_x(OH, F, \ldots)_{2-(x-2u)}$, with $0 \leqslant x \leqslant 2$ and $0 \leqslant 2u \leqslant x$ [1–4]. These compounds are non-stoichiometric, with vacancies in cationic and monovalent anionic crystallographic sites. However, in the last decades it has been shown that bone mineral crystals exhibited, on the surface of their constitutive nanocrystals, a hydrated layer [1–5] mostly containing divalent ions such as Ca^{2+}, CO_3^{2-} and HPO_4^{2-}. The high reactivity of biological and synthetic nanocrystalline apatites (ion exchanges, protein adsorption, etc.) is thought to be directly linked to interactions of this structured (but unstable) layer with the surrounding body fluids [3,4].

Nanocrystalline apatites can be used for the preparation of bioceramics such as bioactive coatings, cements and bulk synthetic ceramics. In the case of bulk biomaterials, the processes used for their preparation generally involve severe sintering conditions such as high temperature (e.g. 1000 °C or higher) and long heating periods (several hours). Such treatments are known to strongly alter the physico-chemical characteristics of the initial powders and particularly their surface reactivity (and therefore their biological activity once implanted in vivo) [2,6,7]. In addition, non-stoichiometric apatites have been shown to decompose irreversibly at temperatures between 500 and 800 °C.

In such severe conditions, hydrated phases are bound to lose their constitutive water. Also, the nanocrystals that may be present before sintering are likely to grow critically in size during the heating process, resulting in a drastic drop in specific surface area. These considerations illustrate the limits of the traditional sintering methods and suggest that other techniques should be investigated, especially when highly reactive hydrated phases are involved.

Spark plasma sintering (SPS) is a relatively new processing technique used for the sintering of various kinds of materials including ceramics, metals, polymers, and composite materials [8]. The heating is obtained by the Joule effect caused by a pulsed direct current (DC) passing through a graphite matrix (die) containing the sample. This process enables fast heating and cooling rates, thus limiting uncontrolled crystal growth, and the sintering temperatures under

Corresponding author. Tel.: +33 562 885 760; fax: +33 562 885 773.
E-mail address: david.grossin@ensiacet.fr (D. Grossin).

SPS conditions are often lower than those used in conventional methods [8].

In the biomedical field, some authors have used SPS to sinter stoichiometric HAP [9–14] and for post-treating HAP-based plasma-sprayed coatings so as to increase their bioactivity [15]. Composites involving HAP associated with yttria or zirconia were also elaborated by SPS in order to improve mechanical properties [16]. Another use of SPS related to biomedical engineering concerned the preparation of transparent β-TCP ceramics [10,17]. More recently, Drouet et al. [18,19] have shown the possibility of consolidating nanocrystalline apatites by SPS at low temperature (⩽200 °C) and pointed out the interest in investigating it in further detail.

The above-cited contributions gave appealing results concerning the use of SPS in the biomaterials field, and have opened interesting perspectives for the consolidation of biomimetic apatites by this technique. The aim of the present contribution was to examine more precisely and in a systematic way the possibilities opened by spark plasma sintering for the consolidation of nanocrystalline apatites at low temperature (lower than 300 °C). This work is focused on the thorough physico-chemical characterization of the consolidated bioceramics obtained, in comparison to the starting powder, in view of a better understanding of the consolidation mechanisms involved.

2. Materials and methods

2.1. Synthesis of apatite powders

Non-carbonated nanocrystalline apatites, $Ca_{10-(x-u)}(PO_4)_{6-x}(HPO_4)_x(OH)_{2-(x-2u)}$, were synthesized by double decomposition [4] between a calcium nitrate solution (prepared with $Ca(NO_3)_2{\cdot}4H_2O$) and a di-ammonium hydrogenphosphate solution in excess (prepared with $(NH_4)_2HPO_4$). The calcium solution was rapidly poured into the phosphate solution at room temperature (20 °C) and stirred for a few minutes. The large excess of phosphate ions in the solution provided pH buffering at a physiological pH of 7.4 during the whole synthesis process. After precipitation, the apatite samples were left to mature in the mother solution (aging) for one day at room temperature, without stirring, to better approach biomimetic conditions, and in a closed vial to minimize the uptake of CO_2. After maturation [2], the precipitate was filtered, thoroughly washed with deionized water, freeze-dried and stored at low temperature (−18 °C). These two last steps were used for limiting possible alterations of the hydrated nanocrystals.

2.2. Spark plasma sintering (SPS)

The spark plasma sintering experiments were performed on SPS 2080 Sumitomo Coal Mining equipment. This device consists of a uniaxial press with a maximum force of 200 kN and a power supply capable of producing a pulsed DC current with a maximum of 8000 A at 10 V. In the present investigation, DC current was limited to 4000 A and a pulse pattern of 12:2 was always used (meaning 12 pulses of 3.3 ms followed by 2 steps of 3.3 ms with no current).

Apatite powder samples (8.5 g) were placed in a 36-mm graphite die. Thin graphite sheets (Papyex®) were used between the powder and the die to facilitate the removal of the consolidated sample. The filled die was then introduced in the treatment chamber under low mechanical pressure in order to ensure electrical contact of the system. The initial green density was close to 0.35 g cm^{-3}. The treatment chamber was purged twice under vacuum and then 1 atm argon pressure was applied during the sintering/consolidation process. The temperature and pressure programmed sequences are described in Fig. 1.

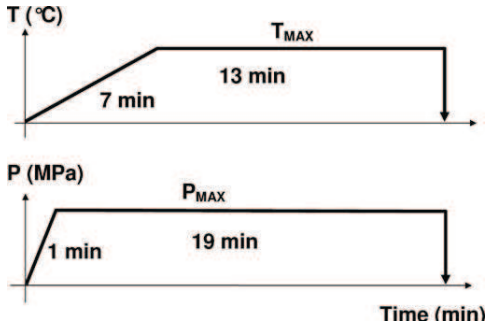

Fig. 1. Schematic, temperature and pressure programmed sequences.

2.3. Sample characterization

Both initial powders and consolidated materials were characterized in this work.

X-ray diffraction (XRD) was used to determine the crystal structure of the samples, using a Siemens diffractometer D5000 with a Cu $K_{\alpha1}K_{\alpha2}$ radiation. For complementary identification, Fourier-transform infrared (FTIR) spectra were recorded on a Nicolet 5700 spectrometer, using the KBr pellet method, in the range 400–4000 cm^{-1} (resolution 4 cm^{-1}). Raman spectra were recorded on a Jobin Yvon HR 800 spectrometer, from 100 to 3800 cm^{-1}, with a laser excitation wavelength of 632.8 nm. Specific surface areas were measured by the Brunauer–Emmett–Teller (BET) method with a Quantachrome Monosorb apparatus. Pore diameter after consolidation was measured with an Hg porosimeter (Micromeritics Autopore 9215). The sample microstructures were investigated by field emission gun scanning electron microscopy (FEG-SEM) (JEOL 7400) equipped with a Gatan Alto 2800 cryogenic system.

3. Results and discussions

3.1. Characterization of initial powder

The purity of the synthesized nanocrystalline apatite powder was checked by XRD (Fig. 2a). The XRD pattern obtained is similar to those obtained in previous works [1,2,4], and corresponds to a poorly crystallized nanocrystalline apatite, as for bone mineral. The diffraction peaks were indexed in reference to the hexagonal structure of HAP given in the ICDD PDF card 9-432. The peak widths reveal a poor crystalline state and/or the nanometer dimensions of the particles, and depend on the crystallographic orientation (e.g. the texture) which underlines the anisotropy of grain size: (0 0 2) (0 0 4) or (0 0 *l*) peaks are thinner than (*h k* 0) ones. The nanometer dimensions (length ≈ 100 nm width ≈ 20 nm) and anisotropy (ratio ≈ 5) of the particles were also observed by cryo FEG-SEM (Fig. 3a). BET measurement revealed a high specific surface area close to 100 m^2 g^{-1}. The Ca/P molar ratio, calculated after calcination at 1000 °C for 15 h [4] is close to 1.51. This value, noticeably below the value 1.67 observed for stoichiometric HAP, stresses the non-stoichiometric nature of the apatitic phase thus prepared.

The FTIR spectrum was recorded on the starting powder. Fig. 4a shows the characteristic absorption bands of a (non-carbonated) non-stoichiometric nanocrystalline apatite) [1,4,22–25], with (i) rather poorly resolved phosphate bands at 474 cm^{-1} (ν_2 PO_4^{3-}), 570 and 601 cm^{-1} (ν_4 PO_4^{3-}), 960 cm^{-1} (ν_1 PO_4^{3-}), 1030 and 1081 cm^{-1} (ν_3 PO_4^{3-}), 1140–1150, 1250 and 875 cm^{-1} (ν HPO_4^{2-}); (ii) the absence of sharp/intense OH^- bands at 630 and 3570 cm^{-1}; and (iii) the observation of water bands at 3000–3400 and 1630 cm^{-1}. Special attention was dedicated to the analysis of the absorption domain around the ν_4 PO_4^{3-} vibration mode. Indeed,

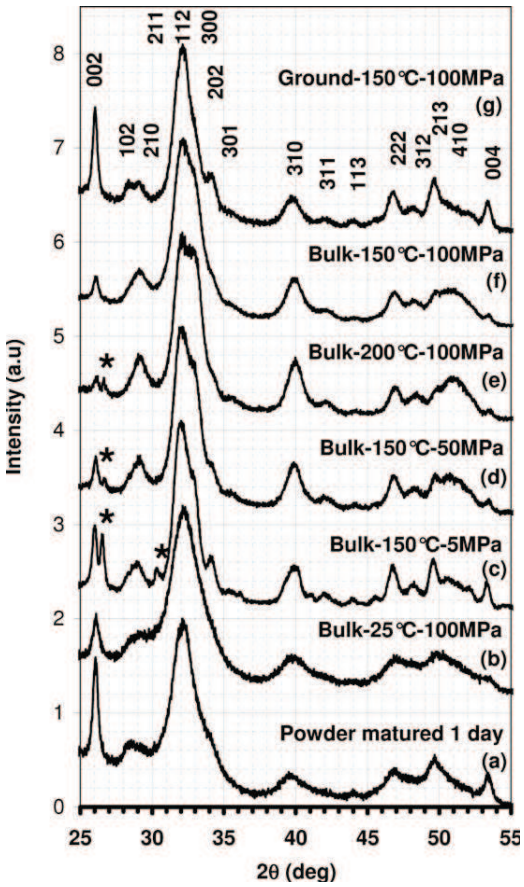

Fig. 2. Diffraction patterns at various sintering conditions. Indexed peaks correspond to hydroxyapatite and those with ∗ to monetite.

this region was shown in earlier studies [1,4,21,23] to include additional phosphate bands which were assigned to non-apatitic chemical environments (not present in well-crystallized stoichiometric HAP). Such non-apatitic environments were linked by Rey et al. [2,4,7] to the presence of hydrated layer on the surface of the nanocrystals, and this hydrated layer is thought to play a key role [3,4] in the biological activity of apatite-based materials. The Raman spectrum of the powder was also recorded and is shown in Fig. 5a. Vibration bands characteristic of apatite were observed at 432 and 452 cm^{-1} (ν_2 PO_4^{3-}), 584, 590 and 611 cm^{-1} (ν_4 PO_4^{3-}), 961 cm^{-1} (ν_1 PO_4^{3-}), 1005, 1030 and 1081 cm^{-1} (ν_3 PO_4^{3-}) and 3570 cm^{-1} (ν OH^-). Very interestingly, a close examination of the ν_1 PO_4^{3-} Raman band, the most intense band, revealed (Fig. 5) a clear asymmetry of the peak, betraying the presence of a shoulder around 955 cm^{-1}, which could reasonably be attributed to the vibration of phosphate groups localized in non-apatitic chemical environment [20,24–26] since this band is not seen in stoichiometric HAP.

Based on the above considerations, special attention has been dedicated to follow FTIR and Raman spectroscopic features in order to check the presence and preservation, after consolidation, of non-apatitic environments associated with the hydrated layer on the nanocrystals (which confers a high surface reactivity).

3.2. SPS processing

3.2.1. Influence of the dwell temperature

The dwell temperature during SPS was the first parameter to be investigated in order to follow its influence on the physico-chemical properties of the consolidated apatite samples. For these experiments, the mechanical pressure was fixed at 100 MPa (101.6 kN) and several temperatures were tested: 25, 75, 100, 125, 150, 200, 250 and 500 °C. The samples prepared were then named following the notation S"temperature"C-"pressure": for example a sample obtained after SPS treatment at 150 °C and 100 MPa is referred to as sample "S150C-100".

Samples obtained (before graphite elimination) are shown in Fig. 6a. The shrinkage vs. the temperature of each sample was recorded (Fig. 7), and two phenomena were systematically evidenced: (i) a first shrinkage (−65%) corresponding to powder reorganization linked to the application of the mechanical pressure, and (ii) most interestingly a second phenomenon observed in the range 100–175 °C leading to a final shrinkage close to 78%. This second, separate phenomenon can reasonably be linked to a sintering/consolidation process, as discussed in Section 3.2.3.

XRD analyses indicated that samples heated at temperatures lower than 200 °C were single-phased apatites (Fig. 2b and f). In contrast, for samples treated by SPS at temperatures higher than or equal to 200 °C, the presence of monetite $CaHPO_4$ (also referred to as DCPA, JCPDS No. 9-80) was detected as a minor secondary phase (peak at $2\theta = 26°$, Fig. 2e).

FTIR spectra obtained for the samples S25C-100 (Fig. 4b) and S100C-100 (Fig. 4c) were found to be highly similar to the spectrum of the starting powder (Fig. 4a). A detailed spectral analysis of the ν_4 PO_4^{3-} vibration region indicated the presence of characteristic shoulders at 500–550 cm^{-1} that can be attributed to HPO_4^{2-} non-apatitic ions, therefore confirming the remaining presence of a hydrated surface layer for those samples. For S125C-100 (Fig. 4d), S150C-100 (Fig. 4e) and S200C-100 (Fig. 4f), similar observations were made concerning the conservation of a hydrated layer. However, differences appeared at 630–635 cm^{-1}, corresponding to the vibration of apatitic OH^- ions, where an increased absorption was found when increasing the SPS dwell temperature (also observed for the OH^- peak at 3570 cm^{-1}). These observations reveal some slight modifications on the composition of the apatitic domains of the nanocrystals. For temperatures higher than or equal to 200 °C, the presence of traces of pyrophosphate ions $P_2O_7^{4-}$ was also detected at 725 cm^{-1} (Fig. 4f for S200C-100).

Raman analyses (Fig. 5) confirmed the FTIR spectral observations for the above-cited samples: (i) a band at 3570 cm^{-1} related to apatitic OH^- ions, with an intensity increasing with the dwell temperature, and (ii) a shoulder at 955 cm^{-1} assignable to non-apatitic phosphate groups (not observed for well-crystallized, stoichiometric apatites), confirming the conservation of the hydrated layer. In addition, Raman analyses allowed us to follow the relative extent of the hydrated layer as well as the hydroxylation of the apatitic phase. For this purpose, an adaptation of the method used by Nelson et al. for carbonate apatites [24,25] was used. Raman spectra were fitted to extract the corrected area of each typical vibration. Two indexes were then calculated: (i) a "hydrated layer" index (HLI) was drawn from the ratio between the non-apatitic ν PO_4^{3-} peak area (955 cm^{-1}) and the ν_1 PO_4^{3-} area (961 cm^{-1}), and (ii) a "hydroxylation index" for apatite (OHI) calculated from the ratio between the ν OH^- area (3570 cm^{-1}) and the ν_1 PO_4^{3-} area (961 cm^{-1}). The variations of HLI and OHI vs. the dwell temperature are shown, respectively, in Fig. 8b and c. The HLI curve can be separated into two domains: a first domain for temperatures in the range 25–100 °C where the index HLI is constant, around 0.35, showing that the hydrated layer remains stable and not degraded, and a second domain, beyond 100 °C, where the HLI index sharply decreases, revealing the alteration of the nanocrystal's hydrated layer. Critical temperatures for this degradation appear to be in the range 100–125 °C. The OHI curve also shows two distinct domains: between 25 and 100 °C a first constant value of OHI is found (close to 0.03), which corresponds to the stability of

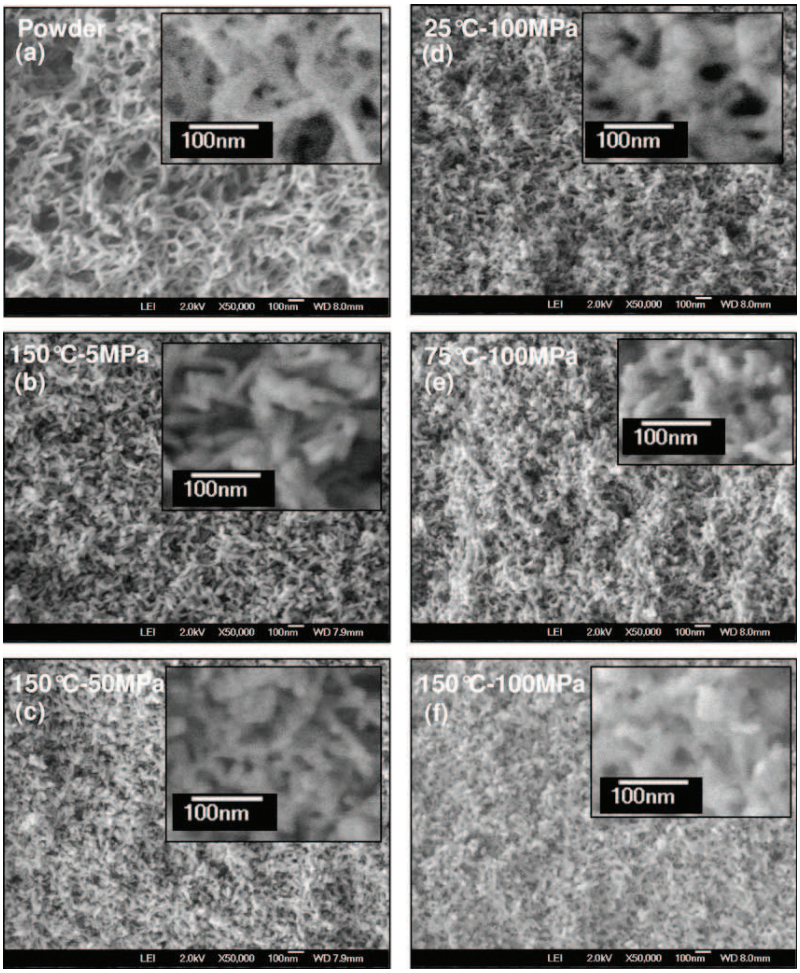

Fig. 3. SEM micrographs performed on samples: (a) powder, (b) sample S150C-5, (c) sample S150C-50, (d) sample S25C-100, (e) sample S75C-100, (f) sample S150-100.

the HLI index (and therefore of the non-stoichiometric apatitic domains), and a second domain above 100 °C where the OHI index progressively increases with temperature. This second phenomenon points out the increase of the amount of apatitic OH^- ions in the samples. It witnesses internal modifications within the nanocrystals due to the temperature rise, with a growth of apatitic domains (present in the core of the crystals) at the expense of the surface hydrated layer.

The weight loss related to the elimination of water during SPS sintering was also followed (Fig. 8d). Indeed, water molecules appear essential for the stability of the hydrated layer. The weight loss curve can be decomposed into 3 parts: (i) from 25 to 75 °C no loss was detected and the sample phase was found to be similar to the initial powder phase; (ii) from 100 to 150 °C a weight loss close to 1% was observed, coinciding with the degradation of the hydrated layer and the increased hydroxylation of the apatite phase observed above (see previous section) although no other phase was detected at this stage; and (iii) from 150 to 500 °C an increasing weight loss was observed (from 1% to 8%), associated in part to the condensation of HPO_4^{2-} ions and the formation of pyrophosphates ions at temperatures above 200 °C (see Figs. 2 and 6). It has been shown that calcium pyrophosphate $Ca_2P_2O_7$ can form by thermal decomposition of monetite [28] (Reaction (1)), corresponding to a water release:

$$2CaHPO_4 \rightarrow Ca_2P_2O_7 + H_2O \quad (1)$$

This reaction corresponds to the observation of calcium pyrophosphate in the FTIR spectra; however, it accounts for ≈1% of the water loss assuming that all HPO_4^{2-} ions have transformed into pyrophosphates. Thus most of the water loss in this temperature range can be assigned to residual water molecules associated with the hydrated layer and some water molecules trapped in the structural defects of the apatite lattice.

The bulk density of the consolidated samples is shown in Fig. 9 as a function of the SPS dwell temperature. The density of the starting non-stoichiometric apatite powder was first measured by helium pycnometry (2.53 g cm^{-3}). The green densities of the samples were close to 0.35 g cm^{-3}. An increase in density was observed with temperature from 75 to 200 °C (2.3 g cm^{-3} at 200 °C). After treatment at 200 °C, the density stabilized at 2.3–2.4 g cm^{-3}.

The microstructure of selected samples was investigated by cryo FEG-SEM. Micrographs of the starting powder and consolidated samples S25C-100, S75C-100, S150C-100 are shown on Fig. 3a, d, e and f, respectively. The decrease in porosity observed as a function of the dwell temperature confirmed the densification previously measured. The observations of grains and nanostructure were, however, difficult because of the resolution limit of the microscope, so that grain size could not be measured precisely. Nevertheless, no grain growth was observed, but we noticed some modifications of grain shape: the rice-like morphology observed for the starting powder gave way to more rounded particles after sintering at 75 °C. This microstructure change could be the result

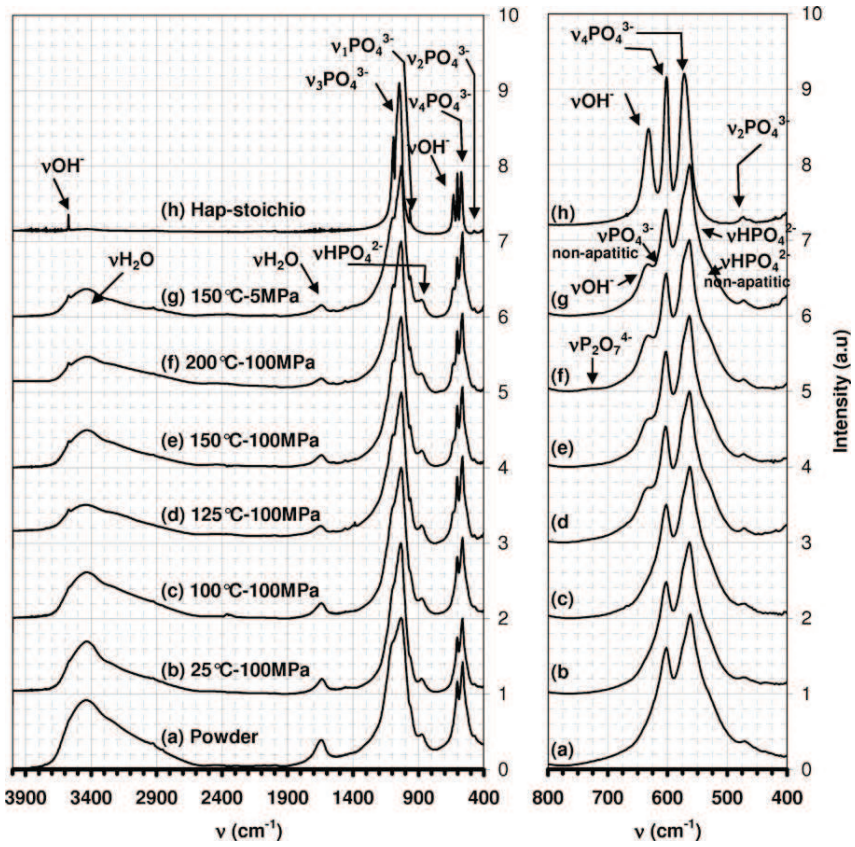

Fig. 4. FTIR spectra of: (a) initial powder, (b) sample S25C-100, (c) sample S100C-100, (d) sample S125C-100, (e) sample S150C-100, (f) sample S200C-100, (g) sample S150C-5. (a) Stoichiometric hydroxyapatite.

of two possible mechanisms: (i) the decomposition of the particles and/or (ii) their mechanical fracture. Further, more detailed microstructural investigations will be performed in order to conclude on this point.

X-ray diffraction (Fig. 2) carried out on the surface of the consolidated samples allowed us to obtain some determining microstructural information. Peak widths revealed low-crystallinity levels and/or the nanometer dimensions of the particles preserved after SPS sintering. Peaks widths were also found to depend on crystallographic orientation, which underlined the anisotropy of grain size (peaks (0 0 2) (0 0 4) or (0 0 *l*)) narrower than (*h k* 0)). Some peak intensities were found to systematically depart from those given in ICDD PDF card 9-432, suggesting a texturation effect after SPS treatment. This point was confirmed by the good agreement obtained for peak intensities after grinding the samples (see Fig. 2a, f and g). Preferred orientations were evidenced at $2\theta = 26°$ (0 0 2), at $2\theta = 33°$ (3 0 0), at $2\theta = 39.5°$ (3 1 0) and at $2\theta = 53.5°$ (0 0 4). In order to estimate the textural effect, a texture index (TI) was calculated (Fig. 9) from the ratio of the peak area for line (0 0 2) and peak area for line (3 1 0). In these conditions, a low value of TI corresponds to crystallite *c*-axis parallel to the surface of the sample, and a high value corresponds to crystallite *c*-axis perpendicular to the sample surface. An important decrease of TI was observed (Fig. 9b) from 75 °C to 125 °C, indicating that the crystallite *c*-axis (corresponding to the larger dimension of the grain) was more and more oriented parallel to the surface sample. The unidirectional pressure applied during SPS treatment is indeed bound to enhance such a textural effect, as the mechanical pressure will favor an orientation of the larger dimension of the grains (length) perpendicularly to the applied force (i.e. parallel to the surface of the sample).

BET specific surface area after consolidation (Fig. 9c) was also followed, and was found to decrease steeply with the SPS dwell temperature until 200 °C, after which a stabilization of the surface area was found. Such a decrease in BET surface areas was already observed on apatite compounds by other authors [29,30] but they attributed this reduction to the removal of impurities generated by chemical synthesis. In our case, we have previously demonstrated the stability of the nanocrystal's hydrated layer at temperatures lower than 100 °C (at 100 MPa), and in this temperature range 25–100 °C, no weight loss was recorded. The decrease in surface area could be here attributed to the development of solid–solid interfaces.

3.2.2. Influence of the mechanical pressure

In these experiments, the dwell temperature was set to 150 °C and different values of the mechanical pressure were selected: 5, 25, 50 and 100 MPa (101.6 kN). Fig. 6b shows the obtained samples (before graphite elimination). The shrinkage observed as a function of time was registered, as previously, for each experiment (Fig. 10). As for the temperature study, two phenomena were also observed here: (i) a shrinkage during the first minutes corresponding to powder reorganization, and (ii) a second shrinking phenomenon starting at $t = 360$ s (corresponding to 130 °C), which could be linked to a sintering at low temperature. Those two phenomena were found to be dependent upon the applied pressure, their variations being in opposite directions: increased mechanical pressures led to a stronger effect for the first shrinking step while the second one decreased. Similar behaviors were already observed in the literature [10] when sintering under pressure was carried out.

XRD analyses performed on the surface of the consolidated samples (Fig. 2) indicated that the samples sintered at 100 MPa

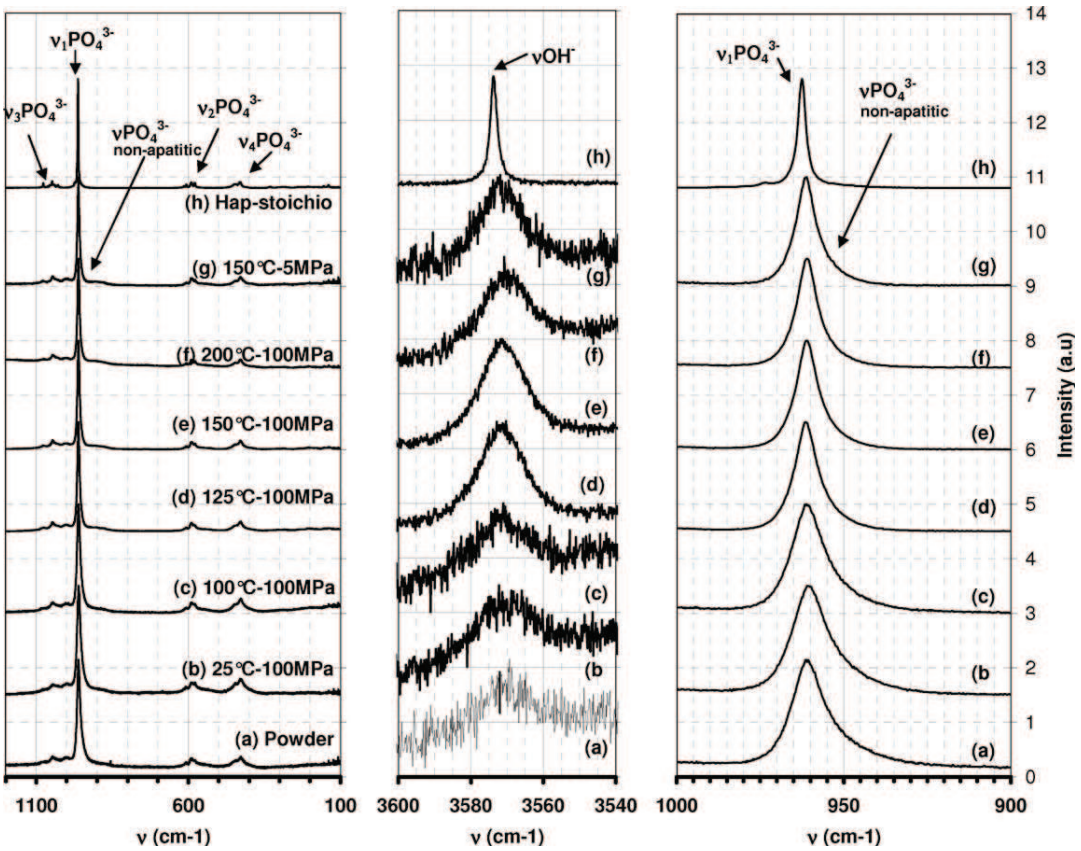

Fig. 5. Raman spectra of: (a) initial powder, (b) sample S25C-100, (c) sample S100C-100, (d) sample S125C-100, (e) sample S150C-100, (f) sample S200C-100, (g) sample S150C-5. (a) Stoichiometric hydroxyapatite.

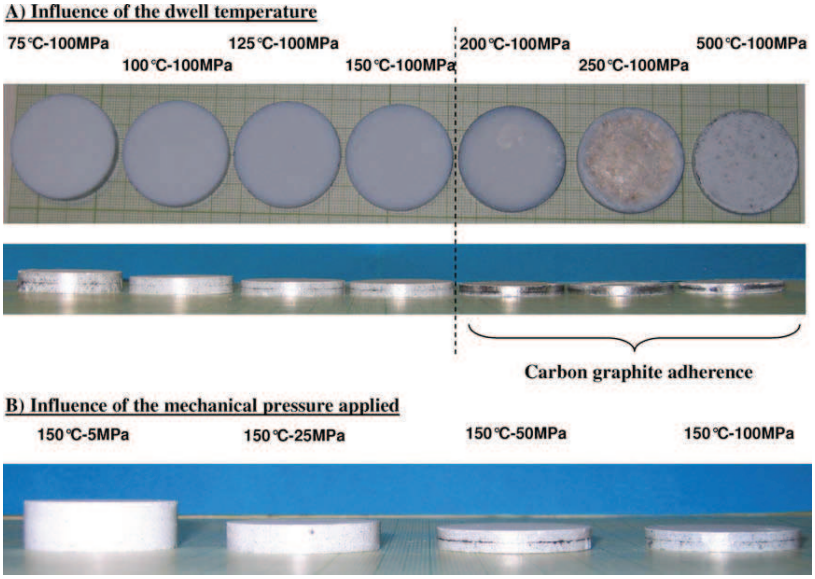

Fig. 6. Macrographs of the as-prepared samples.

(at 150 °C) only showed a low-crystallinity apatite phase (Fig. 2f). On the contrary, traces of monetite $CaHPO_4$ (DCPA) were found on samples sintered at lower pressures (peak at $2\theta = 26°$, Fig. 2c and d), the amount of monetite increasing for decreased applied mechanical pressures.

Those observations were quite unexpected and were then investigated in further detail. FTIR spectroscopy performed on samples S150C-5 (Fig. 4g), S150C-100 (Fig. 4e) showed highly similar spectra, pointing out some hydroxylation (ν OH^- band 630–635 cm^{-1}) as compared to the starting powder. Monetite was not observed

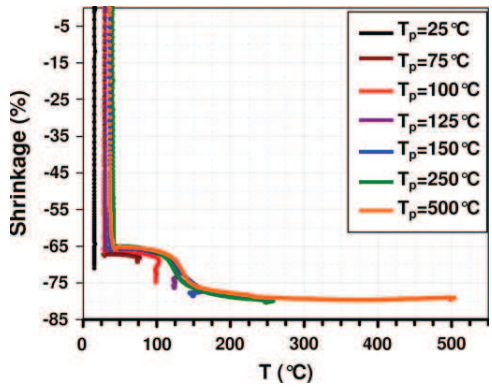

Fig. 7. In situ shrinkage vs. temperature of samples prepared at 100 MPa.

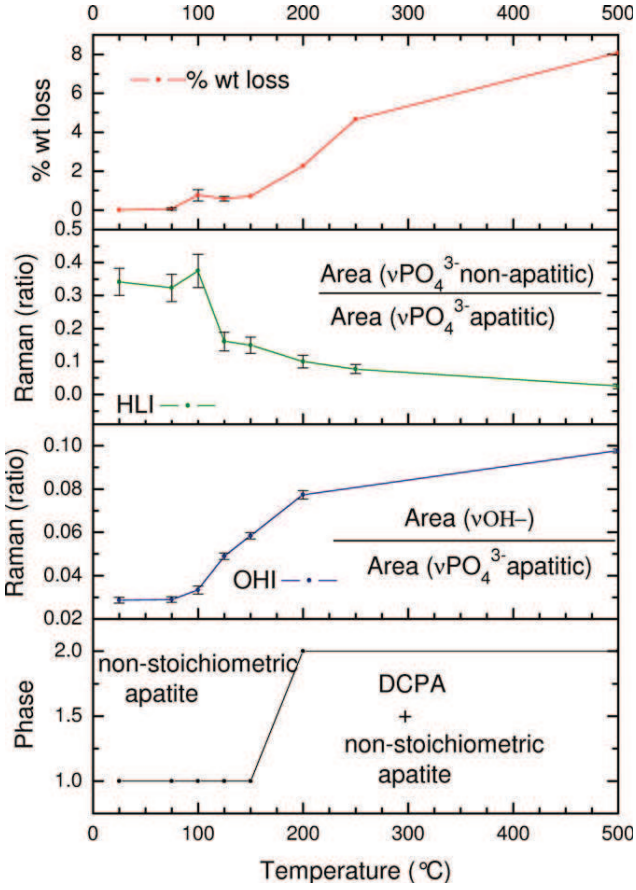

Fig. 8. Variation vs. dwell temperature of (a) weight loss, (b) hydrated layer index HLI, (c) hydroxylation of apatite index OHI, (d) phase occurrence.

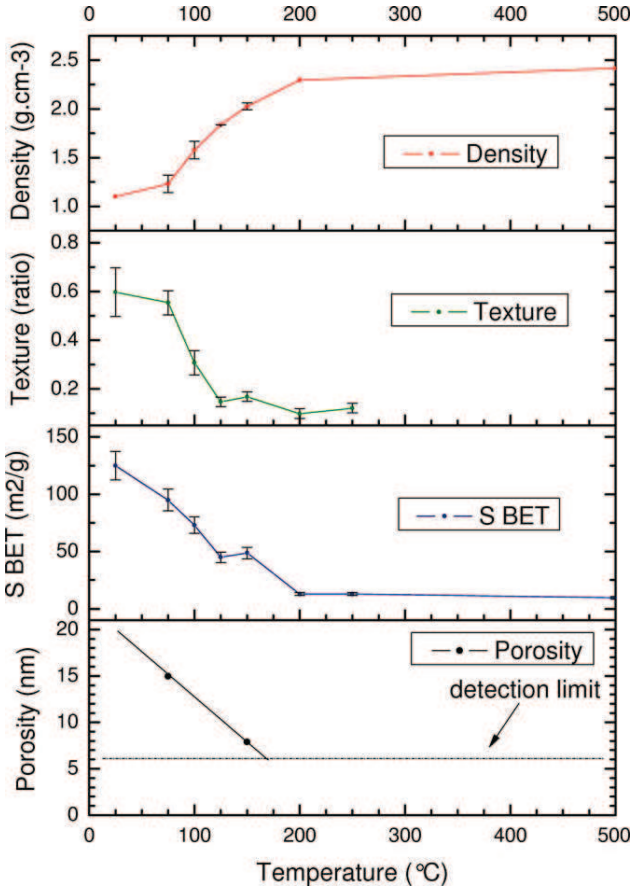

Fig. 9. Variation vs. dwell temperature of (a) density, (b) texture index, (c) BET specific surface area, (d) pore diameter.

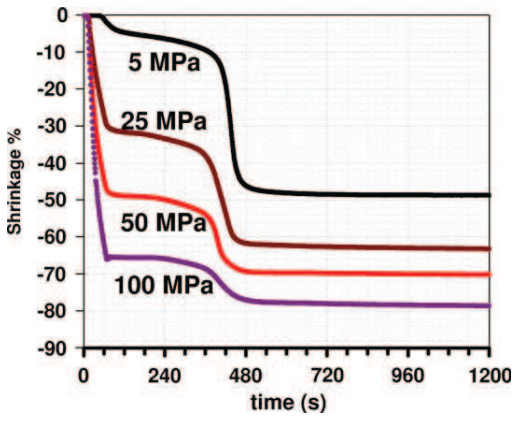

Fig. 10. In situ shrinkage vs. time of samples prepared at 100 MPa.

on the FTIR spectra despite its clear presence in the XRD diffractograms of sample S150-5. In fact, monetite appears difficult to detect by FTIR spectroscopy in the simultaneous presence of apatite.

The two Raman indexes (HLI and OHI) previously described were also calculated for each applied pressure (Fig. 11), but these parameters were only weakly influenced by pressure variations, indicating that pressure (in the observed range) had only a small effect on the stability of the hydrated layer and on the hydroxylation extent.

The weight loss measured after SPS consolidation was found to decrease (from 3% to 1%) for increasing applied mechanical pressures in the range 5–100 MPa. The high weight losses (>1%) can be mainly attributed to the loss of residual water associated with the hydrated layer as no pyrophosphate formation has been detected.

The variation of the density as a function of the applied pressure is shown in Fig. 12a. An increase of density (0.5–2.1 g cm^{-3}) was observed for pressures from 5 to 100 MPa. The microstructure of some samples was analyzed by cryo FEG-SEM (Fig. 3b, c and f) and compared to the initial powder (Fig. 3a). A decrease in porosity was seen, confirming the density variation previously measured. However, no grain growth was observed although a modification of grain shape was noticed (decreased in anisotropy for increased

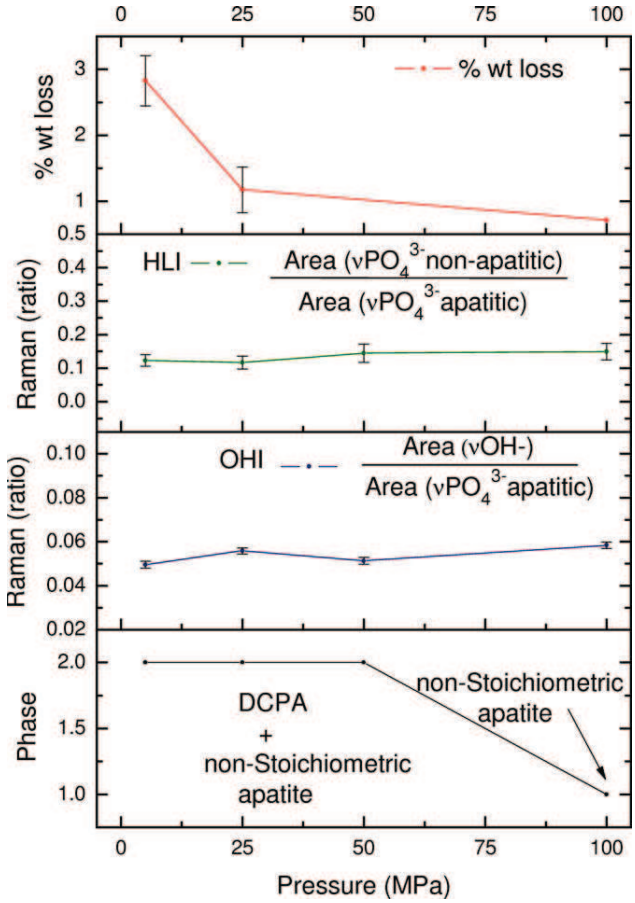

Fig. 11. Variation vs. dwell temperature of (a) weight loss, (b) hydrated layer index HLI, (c) hydroxylation of apatite index OHI, (d) phase occurrence.

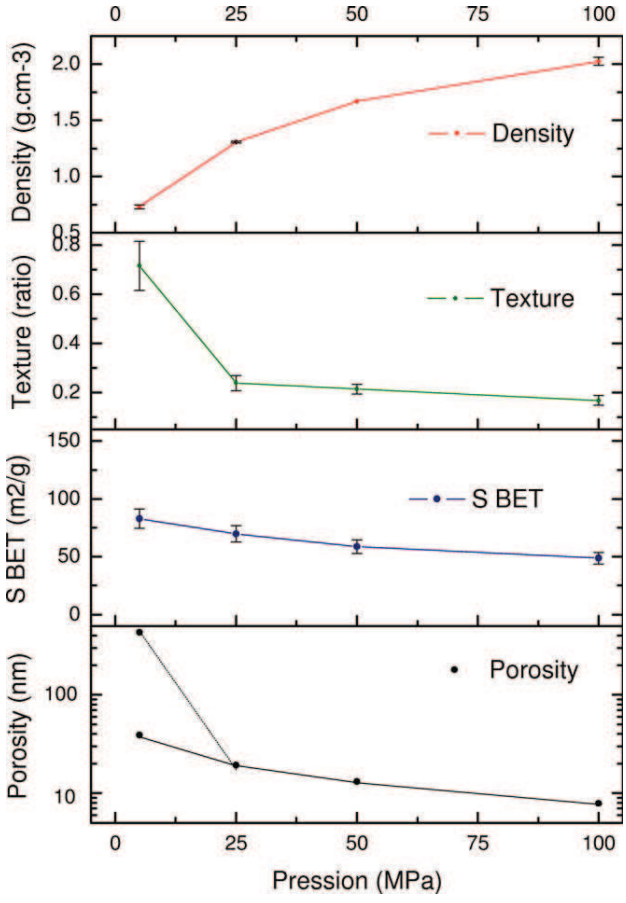

Fig. 12. Variation vs. dwell temperature of (a) density, (b) texture index, (c) BET surface, (d) pore diameter.

pressures), but this modification was very weak at low pressure. The comparison between temperature and pressure effects revealed that the grain morphology was noticeably more influenced by temperature than by pressure.

A microstructural analysis was then drawn from XRD measurements (Fig. 2) for varying pressures, as it was done previously for the effect of the dwell temperature. However, in this case, only slight modifications of the crystallinity state and/or nanometer dimensions of particles, and of the anisotropy of grain size, were noticeable. The value of the texture index TI as a function of the applied pressure is reported in Fig. 12b. A strong decrease of TI was observed from 5 to 100 MPa, revealing for increased pressures a more pronounced orientation of the crystallite *c*-axis in a direction parallel to the surface sample. Such textural effect with pressure is, again, commonly observed when unidirectional pressure is applied on anisotropic grains [8].

BET specific surface areas for consolidated samples were shown to decrease with increasing pressure (Fig. 12c). This observation might be correlated to the decrease in pore diameters, as surface and pore size are generally linked. Pore diameters were also measured on each sample. The diameter at maximum Hg intrusion was drawn as a function of the SPS applied pressure (Fig. 12d). The pore size distributions were monomodal except for the sample S150C-5 for which a bimodal distribution was observed (secondary maximum added in Fig. 12d for 5 MPa). This latter bimodal distribution could be explained by an intra-agglomerate porosity centered at 40 nm (main peak) and an inter-agglomerate porosity around 400 nm (secondary peak). The inter-agglomerate porosity was eliminated for pressures greater than 5 MPa, while the intra-agglomerate pore diameters decreased from 40 to 8 nm with an increase of applied pressure. A reduction of inter-crystalline porosity is one of the advantages of sintering processes performed under mechanical pressure [8,31].

3.2.3. Discussion

Shrinkage phenomena were measured close to 15% between 100 and 160 °C. The decrease in specific surface area and pore diameters were also recorded simultaneously as well as some extent of water loss. Those experimental and reproducible observations suggest strongly the reduction of solid/gas interfaces linked with a sintering effect. Three-point bending tests were carried out on two samples ($30 \times 3.5 \times 4.1$ mm^3) sintered at 150 °C and 100 MPa. Flexural strengths were 16.2 MPa for the first sample and 10.3 MPa for the second sample. These values reveal a rather high mechanical resistance after SPS treatment also accounting for the effectiveness of consolidation and sintering [32,33].

As with all other irreversible processes, sintering is accompanied by a lowering of the free energy of the system. The sources that give rise to this lowering are commonly referred to as the "driving forces for sintering". Conventionally three possible driving forces: curvature of the particle surfaces, externally applied pressure and chemical reaction are involved in high-temperature sintering. These driving forces provide a motivation for sintering but the actual occurrence of sintering requires transport of matter, which in solids occurs by a process of diffusion involving atoms, ions or molecules. However, in our case, at the very low, unconventional temperatures involved, the thermal agitation factors are too weak for involving a direct atom's mobility like in high-temperature sintering, even at

the surface of the material. It appears then that the persistence of a hydration layer is probably the additional feature allowing ion mobility and displacements. In addition to diffusivity allowed by an elevated ion, mobility within the hydrated layer present in the nanocrystals and the nanocrystalline nature of the crystals with many structural defects can also be probably considered. One may hypothesize at this stage that the surface hydrated layer could act as a secondary liquid phase, favoring liquid phase diffusion and sintering, which requires much lower activation energy than solid phase diffusion. However, the exact sintering process has still to be investigated.

4. Conclusions

Nanocrystalline apatites can successfully be consolidated by SPS. The high ion mobility reported previously within the hydrated layer present on such nanocrystalline apatites [3,27] can probably explain the possibility of sintering/consolidating these materials at such low temperatures, since diffusivity is possible without the urgent need for thermally activated diffusion processes. In our case it may mostly involve surface mechanisms similar to liquid phase sintering. We showed that such biomimetic apatites with a preserved hydrated layer could be prepared if sintering conditions (temperature and pressure dwell) were adjusted. First, high pressures are required (e.g. 100 MPa) in order to limit water elimination and monetite formation. Second, at such pressures, the limit temperature (limited acceptable alteration of hydrated layer) was found in the range 150–200 °C.

Microstructure studies revealed the existence of preferred orientations for the acicular grains, and a modification of grain shape (less acicular) upon temperature and/or pressure increase. A reduction of inter- and intra-agglomerate porosity was also evidenced in such conditions.

This physico-chemical study sheds more light on the possibility of consolidating biomimetic apatites by SPS at low temperatures while retaining the initial advantageous characteristics of the powder (nanosized crystals, preserved hydrated layer, non-stoichiometry). It enabled us to follow quantitatively the evolution of several physico-chemical parameters and to distinguish the roles of temperature and mechanical pressure in view of bone regeneration applications. The evaluation of the mechanical and biological properties of such low-temperature consolidated materials is now in progress.

Acknowledgements

This research is supported by the ANR "Agence Nationale de la Recherche" (ref: NanoBioCer: ANR-07-BLAN-0373). Sabrina Rollin-Martinet thanks ANR for financial support of her Ph.D funding. David Grossin is grateful to the CNRS for a post-doctoral fellowship.

Appendix A. Figures with essential colour discrimination

Certain figures in this article, particularly Figs. 6–12, are difficult to interpret in black and white. The full colour images can be found in the on-line version, at doi:10.1016/j.actbio.2009.08.021).

References

[1] Kalita SJ, Bhardwaj A, Bhatt HA. Nanocrystalline calcium phosphate ceramics in biomedical engineering. Mater Sci Eng C 2007;27:441–9.
[2] Rey C, Hina A, Tofighi A, Glimcher MJ. Maturation of poorly crystalline apatites: chemical and structural aspects in vivo and in vitro. Cells Mater 1995;5:345–56.
[3] Cazalbou S, Eichert D, Ranz X, Drouet C, Combes C, Harmand MF, et al. Ion exchanges in apatites for biomedical applications. J Mater Sci Mater Med 2005;16:405–9.
[4] Eichert D, Drouet C, Sfihi H, Rey C, Combes C. Nanocrystalline apatite-based biomaterials: synthesis, processing and characterization. In: Kendall B Jason, editor. Biomaterials Research Advances. Nova Science Publishers; 2007. p. 93–143. ISBN:1-60021-892-x [chapter 5].
[5] Eichert D, Combes C, Drouet C, Rey C. Formation and evolution of hydrated surface layers of apatites. Key Eng Mater 2005;284–286:3–6.
[6] Legeros RZ. Biodegradation and bioresorption of calcium phosphate ceramics. Clin Mater 1993;14:65–88.
[7] Rey C, Strawich E, Glimcher MJ. Non-apatitic environments in Ca–P biominerals; implications in reactivity of the mineral phase and its interactions with organic matrix constituents. In: Allemand D, Cuif JP, editors. Bulletin de L'Institut Oceanographique n° 14: Biomineralizations 93 (Part 1–Fundamentals of Biomineralization). L'Institut Oceanographique de Monaco; 1994. p. 55–64. ISBN 2–7260-0168-8.
[8] Rahaman MN. Ceramic processing and sintering. 2nd ed. Boca Raton, FL: CRC Press; 2003.
[9] Gu YW, Loh NH, Khor KA, Tor SB, Cheang P. Spark plasma sintering of hydroxyapatite powders. Biomaterials 2002;23:37–43.
[10] Kawagoe D, Koga Y, Kotobuki N, Ohgushi H, Hideki Ishida E, Ioku K. Densification behavior of calcium phosphates on spark plasma sintering. Key Eng Mater 2006;309–311:171–4.
[11] Yamaguchi N, Tanaka H, Ohashi O. Gas analysis in spark plasma sintering of hydroxyapatite. Mater Sci Forum 2004;449–452:793–6.
[12] Khor KA, Gu YW, Cheang P, Boey FYC. The characteristics and properties of hydroxyapatite prepared by spark plasma sintering (SPS). Key Eng Mater 2003;240–242:497–500.
[13] Nakahira A, Tamai M, Aritani H, Nakamura S, Yamashita K. Biocompatibility of dense hydroxyapatite prepared using an SPS process. J Biomed Mater Res 2002;62:550–7.
[14] Guo X, Xiao P, Liu J, Shen Z. Fabrication of nanostructured hydroxyapatite via hydrothermal synthesis and spark plasma sintering. J Am Ceram Soc 2005;88:1026–9.
[15] Zhang G, Li Y, Ren S, Zhang J. HA Active coating on titanium prepared by spark plasma sintering. Key Eng Mater 2007;353–358:1679–82.
[16] Moon B-K, Kamada K, Enomoto N, Hojo J, Lee S-W. Effect of calcination on mechanical properties of hydroxyapatite/zirconia composite sintered by spark plasma sintering. Mater Sci Forum 2007;561–565:613–6.
[17] Lin KL, Qin C, Ni SY, Chen LD, Lu JX, Chang J. Fabrication of transparent β-Ca3(PO4)2 bioceramics by spark plasma sintering technique using ultrafine powders. J Inorg Mater 2006;21:645–50.
[18] Drouet C, Largeot C, Raimbeaux G, Estournes C, Dechambre G, Combes C, et al. Bioceramics: spark plasma sintering (SPS) of calcium phosphates. Adv Sci Technol 2006;49:45–50.
[19] Drouet C, Bosc F, Banu M, Céline Largeot C, Combes C, Dechambre G, Estournès C, Raimbeaux G, Rey C. Nanocrystalline apatites: from powders to biomaterials. Powder Technol 2009;190:118–22. doi:10.1016/j.powtec.2008.04.04.
[20] Antonakos A, Liarokapis E, Leventouri T. Micro-Raman and FTIR studies of synthetic and natural apatites. Biomaterials 2007;28:3043–54.
[21] Penel G, Leroy G, Rey C, Sombret B, Huvenne JP, Brès E. Infrared and Raman microspectrometry study of fluor-fluor-hydroxy and hydroxyl-apatite powders. J Mater Sci Mater Med 1997;8:271–6.
[22] Blakeslee CK, Condrate RA. Vibrational spectra of hydrothermally prepared hydroxyapatites. J Am Ceram Soc 1971;54:559–63.
[23] Rey C, Shimizu M, Collins B, Glimcher MJ. Resolution-enhanced Fourier transform infrared spectroscopy study of the environment of phosphate ion in early deposits of a solid phase of calcium phosphate in bone and enamel and their evolution with age: 2. Investigations in the v3 PO4 domain. Calcif Tissue Int 1991;49:383–8.
[24] Awonusi A, Morris MD, Tecklenburg MMJ. Carbonate assignment and calibration in the Raman spectrum of apatite. Calcif Tissue Int 2007;81:46–52.
[25] Nelson DGA, Featherstone JDB. Preparation, analysis and characterization of carbonated apatites. Calcif Tissue Int 1982;34:S69–81.
[26] Nelson DGA, Williamson BE. Low-temperature laser Raman spectroscopy of synthetic carbonated apatites and dental enamel. Aust J Chem 1982;35:715–27.
[27] Daculsi G, Menanteau J, Kerebel LM, Mitre D. Length and shape of enamel Crystals. Calcif Tissue Int 1984;36:550–5.
[28] Lasserre V, Lebugle A. Etude de la decomposition, en atmosphere humide, d'une apatite non-stoechiometrique. Ann Chim Fr 1996;21:205–29.
[29] Ababou A, Bernache-Assollant D, Heughebaert M. Influence des conditions de calcination sur l'evolution morphologique de l'hydroxyapatite. Ann Chim Fr 1994;19:165–75.
[30] Ababou A, Bernache-Assollant D, Heughebaert M. Influence of vapor on grain growth during the calcination of hydroxyapatite. In: Hausner H, Messing GL, Hirano SI, editors. Ceramic transactions, no. 51. Westerville, OH: American Ceramic Society; 1995. p. 111–5.
[31] Nygren M, Shen Z. On the preparation of bio-, nano- and structural ceramics and composites by spark plasma sintering. Solid State Sci 2003;5:125–31.
[32] Pontier C, Champion E, Viana M, Chulia D, Bernache-Assollant D. Use of cycles of compression to characterize the behaviour of apatitic phosphate powders. J Eur Ceramic Soc 2002;22:1205–16.
[33] Raynaud S, Champion E, Lafon JP, Bernache-Assollant D. Calcium phosphate apatites with variable Ca/P atomic ratio III. Mechanical properties and degradation in solution of hot pressed ceramics. Biomaterials 2002;23:1081–9.